Ultra-compact silicon photonic integrated interferometer for swept-source optical coherence tomography

Günay Yurtsever,[1,2,*] Nicolás Weiss,[3] Jeroen Kalkman,[4] Ton G. van Leeuwen,[3] and Roel Baets[1,2]

[1]*Photonics Research Group, Ghent University-imec, Sint-Pietersnieuwstraat 41, B-9000 Ghent, Belgium*

[2]*Center for Nano- and Biophotonics (NB-Photonics), Ghent University, Ghent, Belgium*

[3]*Biomedical Engineering & Physics, Academic Medical Center, University of Amsterdam, P.O. Box 22700, Amsterdam 1100 DE, The Netherlands*

[4]*Department of Imaging Physics, Delft University of Technology, Lorentzweg 1, 2628 CJ Delft, The Netherlands*

**Corresponding author: gunay@intec.ugent.be*

Received June 3, 2014; revised July 23, 2014; accepted August 4, 2014; posted August 4, 2014 (Doc. ID 213214); published August 29, 2014

We demonstrate an ultra-compact silicon integrated photonic interferometer for swept-source optical coherence tomography (SS-OCT). The footprint of the integrated interferometer is only 0.75×5 mm^2. The design consists of three 2×2 splitters, a 13 cm physical length (50.4 cm optical length) reference arm, and grating couplers. The photonic integrated circuit was used as the interferometer of an SS-OCT system. The sensitivity of the system was measured to be −62 dB with 115 μW power delivered to the sample. Using the system, we demonstrate cross-sectional OCT imaging of a layered tissue phantom. We also discuss potential improvements in passive silicon photonic integrated circuit design and integration with active components.

OCIS codes: (110.4500) Optical coherence tomography; (170.4500) Optical coherence tomography; (100.3175) Interferometric imaging; (130.0130) Integrated optics.

http://dx.doi.org/10.1364/OL.39.005228

Optical coherence tomography (OCT) has become a standard tool for retinal imaging in the relatively short time since its invention [1]. During this period, the development of OCT has significantly benefited from the availability of optical fiber components developed for telecom applications. Currently, photonic integration in telecommunications is driven by the increasing demand for higher data bandwidth at a lower cost. Similarly, integrated photonics has the potential to reduce the size and the cost of OCT systems, which can open new opportunities for its deployment in various application areas.

Recently, various approaches to using integrated photonics for OCT have been studied. Akca *et al.* demonstrated an integrated spectrometer and a 2×2 splitter using silicon oxynitride (SiON) waveguides [2], albeit without on-chip integration of the reference arm. Nguyen *et al.* reported a Michelson interferometer using silicon nitride (Si_3N_4) strip waveguides. In this study, the reference arm was realized on chip [3]. However, the relatively short length of the reference arm did not encompass space for a sample arm galvo-scanner, and therefore the sample needed to be scanned to obtain cross-sectional images. More recently, Yurtsever *et al.* reported a Mach–Zehnder interferometer using silicon nitride (Si_3N_4) box-shaped waveguides with a long on-chip reference arm capable of accommodating a galvo-scanner in the sample arm [4].

In recent years, photonic integrated circuits based on silicon have gained substantial interest from the telecom industry. Silicon is one of the most developed material systems for microelectronic fabrication. Hence, using silicon as a platform for photonic integrated circuits enables the use of existing CMOS infrastructure and processing recipes developed for silicon microelectronics fabrication. Wafer-scale fabrication of silicon photonic integrated circuits using CMOS infrastructure [5] significantly reduces the price per chip. In addition to cost advantages, silicon waveguides have a very high confinement factor, which enables much smaller integrated photonic circuits than low-index-contrast material systems. In addition to miniaturization, significant reduction in size can enable faster, parallel OCT systems. Furthermore, several groups have also demonstrated that active components such as lasers, photodetectors, and modulators can be integrated on wafer-scale with silicon waveguides. A broad review of active component integration with silicon waveguides is presented by Park *et al.* [6]. In addition to active components, electronic and photonic integration can be combined on the same material system, which can further miniaturize electro-optical systems [7]. Thus, compared to other integrated photonic material systems, silicon can have a significant potential for mass fabrication of OCT devices, which would result in miniaturization, cost reduction, and wider deployment.

In this study, for the first time to the best of our knowledge, we demonstrate OCT imaging based on a silicon photonic integrated chip. The size of the chip is only 0.75×5 mm^2, which is 90 times smaller than the chip we previously demonstrated in silicon nitride (Si_3N_4) [4]. The chip consists of grating couplers, a 13 cm long (physical length) reference arm, and three 2×2 couplers in a Mach–Zehnder interferometer configuration. Using a swept light source, we obtained cross-sectional OCT images from a layered tissue phantom by scanning the beam with a galvo-scanner. Besides the design and the measurements, we discuss the challenges and potential improvements in silicon photonic integrated circuit design related to OCT imaging.

An illustration of the OCT system used to perform the experiments is shown in Fig. 1(a). Light from a swept source (Axsun Technologies, USA) centered at 1312 nm is coupled into the chip using an SMF-28 fiber array with a 127 μm pitch and 10° polish angle (OZ Optics, Canada). For long-term alignment stability, the fiber array was

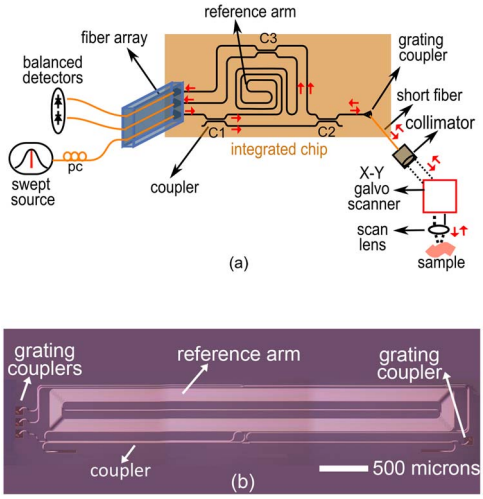

Fig. 1. (a) Schematic of the OCT setup with the photonic integrated circuit, pc: polarization controller; C1, C2, C3: 2×2 couplers. The direction of the light is indicated by red arrows. (b) Microscope image of the fabricated photonic integrated interferometer.

glued to the chip with UV curable glue. Coupling in and out of the chip is achieved with tilted grating couplers with reduced back reflection [8]. Grating couplers provide access to waveguides through vertical coupling. The polarization of the input light is adjusted to the TE-polarization since the grating couplers were designed for TE-light. After entering the chip, the light is split into reference and sample arms via the 2×2 coupler C1. In the sample arm, the light is split again by the 2×2 coupler C2 and finally sent out of the chip with a grating coupler. The light exiting the chip is coupled to a short piece of (2 cm) single-mode fiber (SMF), which is attached to a collimator (F280APC-C, Thorlabs, USA). The light from the collimator is directed to the sample via the galvo-scanner and the scan lens. Back scattered light from the sample is combined on the chip with the light from the reference arm at the 2×2 coupler C3. The combined light at both output arms of the 2×2 coupler C3 leaves the chip via grating couplers. The fibers in the fiber array aligned with these grating couplers send the light to a balanced photodetector (Thorlabs PDB 110C, USA).

A microscope image of the fabricated chip is shown in Fig. 1(b). The single-mode rib waveguides are 470 nm wide, 220 nm high, and the bend radius is 50 μm. The loss of the straight waveguides is measured to be 0.35 dB/cm. The group index of the waveguides is $n_{\text{group}} = 3.88$ and hence the optical length of the reference arm is 50.4 cm. The designed circuit was fabricated on a 200 mm silicon-on-insulator (SOI) wafer consisting of 220 nm thick silicon on top of 2000 nm of buried oxide layer using 248 nm lithography. A single etch step of 70 nm was used for the definition of the waveguides and the grating couplers. To protect the chip from dust it was covered with silicon dioxide as a top cladding by using plasma deposition. The fabrication was performed through a cost sharing multi-project wafer service, ePIXfab silicon photonics platform [9].

To characterize the individual photonic integrated components, we measured the bandwidth of the grating couplers, the 2×2 couplers, and the power levels at the sample and reference arms. The grating couplers have 7.5 dB insertion loss and a 45 nm 3 dB bandwidth. For the 2×2 couplers, we chose to design adiabatic couplers as they have a broader bandwidth than directional couplers. Adiabatic couplers using both rib and ridge silicon waveguides have been experimentally demonstrated [10,11]. In principle, couplers C1 and C2 can be realized using y-splitters, as they are wavelength independent. However, generally y-splitters have higher insertion losses than directional couplers and also cause some back reflection because of fabrication limited blunt at the junction. The length of the 2×2 couplers is 2.1 mm and the gap between the waveguides is 0.7 μm. Because of deviations between the designed and the fabricated geometry, the splitting ratio deviated from simulations; the measured splitting ratio was 45:55 at 1266 nm and 30:70 at 1356 nm.

The swept source has a 50 kHz repetition rate, 92 nm tuning range, and provides −6 dB roll-off at 3.5 mm depth. Each sweep cycle is sampled with 1088 points which corresponds to a 5.09 mm maximum imaging depth. The power delivered to the chip was 12.4 dBm (17.5 mW), while the power on the sample was measured to be −9.4 dBm (115 μW), which means 21.8 dB attenuation compared to the input power. The attenuation results from the losses induced by the two grating couplers and the two 2×2 couplers. The power levels from the reference arm reaching the balanced photodetector were −14.7 dBm (36 μW) and −16.8 dBm (21 μW).

Owing to their lower loss, the rib waveguides in this design (0.35 dB/cm loss) were preferred over ridge waveguides (2 dB/cm loss). However, the dispersion of these waveguides is significant; their group velocity dispersion was simulated to be −1700 ps/(nm·km) at 1310 nm. As dispersion of the reference arm cannot be compensated for in the sample arm, numerical dispersion compensation in software is necessary. For dispersion compensation, we first measured the reflection from a mirror in the sample arm. The measured interference fringe [Fig. 2(a)] shows that the fringe frequency increases strongly with increasing wavelength. The measured bandwidth of the interference is reduced, compared to the source bandwidth because of the bandwidth of the grating couplers, which limits the axial resolution to 24.4 μm (FWHM) (obtained from the Fourier transform of the envelope of the interference signal). On the other hand, without dispersion compensation, the Fourier transform of the interference resulted in 1231 μm axial resolution as shown in Fig. 2(b). To compensate for dispersion, we found the dispersion coefficients by fitting a third order polynomial to the phase obtained from the interference. After third order dispersion compensation [12], 25.5 μm axial resolution was obtained as shown in Fig. 2(b). Compensation for dispersion orders higher than the third order did not further improve the axial resolution. The axial resolution of a fiber-based OCT system using the same laser was 12.5 μm [13]. It should be noted that if the sample is placed close to the maximum imaging depth, aliasing will occur because of the large dispersion. The aliased signals cannot be compensated for dispersion and axial

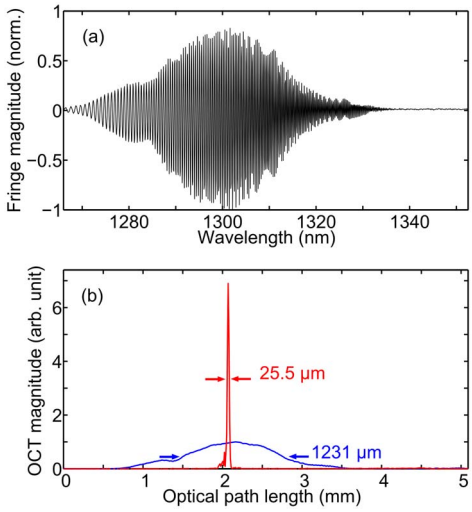

Fig. 2. (a) Interference fringe for a reflection from a mirror. (b) Fourier-transform of the interference signal, before (blue) and after (red) dispersion compensation. The peak of the blue line is normalized to 1.

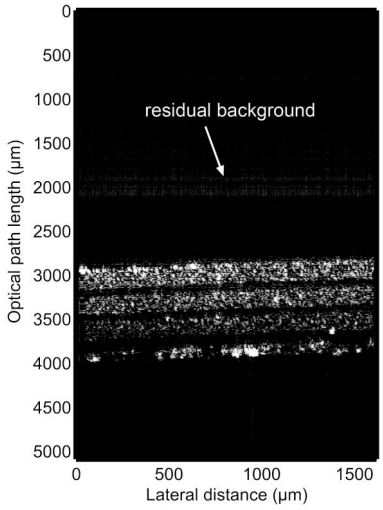

Fig. 3. OCT cross-sectional image (average of 100 B-scans) of a layered tissue phantom.

resolution and OCT signal amplitude near the maximum imaging depth will be degraded [14].

To characterize the sensitivity of the system, we placed an OD 1.2 neutral density filter in the sample arm and measured the reflection from a mirror. The sensitivity of the system was calculated by the ratio of the amplitude of the OCT signal peak to the standard deviation of the noise floor. The sensitivity of the system with 115 μW power on the sample was measured to be −62 dB. We also measured the sensitivity of the fiber-based SS-OCT system [13] as −84 dB, using the same swept source, reference and sample arm powers, galvo-scanner, photodetector, and analog-to-digital converter card settings. Thus, the chip-based system had a 22 dB lower sensitivity than the fiber-based system. The degradation of the sensitivity can be explained mainly by the insertion losses in the grating couplers and an additional 3 dB loss of the 2×2 coupler C2 (while reflected light from the sample passes through the 2×2 coupler C2 and goes toward the photodetectors). Additionally, the 2×2 couplers of the fiber SS-OCT system (FC1310-70-50-APC, Thorlabs, USA) were significantly more wavelength independent than the on-chip 2×2 couplers and thus are better suited for balanced detection resulting in improved common mode noise reduction.

To demonstrate OCT imaging with the chip-based system, we imaged a three-layer tissue phantom as shown in Fig. 3. The scattering layers of the phantom had a scattering coefficient $\mu_s = 4\ \text{mm}^{-1}$, a refractive index $n = 1.41$, and were separated by nonscattering tape [3]. The image was obtained by averaging 100 B-scans. Near the middle of the image, a faint residual background signal as a result of internal reflections in the chip is seen. Because of laser power and phase fluctuations between each A-line, the background signal could not be completely removed by background subtraction. The residual background signal was observed only with the chip-based system, and is absent in the fiber-based system. The phantom was placed slightly away from the residual background signal to prevent overlapping.

Although we demonstrated OCT imaging using the chip-based system, the sensitivity and axial resolution are relatively low compared to state-of-the art OCT systems. However, the sensitivity and the axial resolution can be significantly improved using more advanced fabrication methods to fabricate fiber to chip coupling structures with lower insertion loss and larger bandwidth. Simple grating couplers used in this study are easy to fabricate but are not the optimum solution. By using more advanced fabrication processes, grating couplers with 1.6 dB loss and 80 nm 3 dB bandwidth have been demonstrated [15]. For even larger bandwidths, a solution is to use horizontal butt-coupling using spot size converters to couple the light in and out of the chip. Spot size converters gradually enlarge the mode size in the waveguide and are usually fabricated as tapered waveguide structures. Ben Bakir *et al.* demonstrated 3×3 μm spot size converters with >200 nm bandwidth and 1 dB insertion loss [16]. Coupling efficiently to such a small spot size converter with a lensed fiber is feasible. However, based on our experience, coupling efficiently to multiple adjacent small spot size converters may not be practical because of fabrication tolerances in lensed fiber arrays. Thus, spot size converters with low-loss coupling to standard SMFs are desirable. Shiraishi *et al.* demonstrated a spot size converter with 2.8 dB coupling loss to a standard SMF [17]. Further research on SMF spot size converters would increase the coupling tolerances and reduce packaging costs, and improve OCT performance.

In general, high index contrast integrated waveguides are much more dispersive than SMFs; however by changing the width and height of the waveguides or the cladding material, dispersion could be reduced. Through simulations, we observed that using ridge waveguides rather than rib waveguides provides more flexible dispersion tailoring. For example, we simulated that an SOI, SiO_2 cladding ridge waveguide with 220 nm height and 540 nm width would have zero group velocity dispersion at 1310 nm. Although rib waveguides have higher losses than ridge waveguides, their loss could be reduced to 0.45 dB/cm by using higher resolution lithography [5].

The return loss of individual components in a photonic integrated circuit for OCT is also crucial. The return loss of fiber components which are connected to each other with fibers much longer than the coherence length of the light source does not present a significant problem. However, the distances between individual components in a photonic integrated chip are in the order of the coherence length of OCT light sources. Thus, fringes resulting from reflections within the chip may appear as spurious background signals in the OCT signal. To avoid this, the transition between different photonic integrated components needs to be sufficiently smooth to reduce such reflection effects.

For Fourier-domain OCT implementation, currently silicon is more appropriate for SS-OCT than spectral-domain OCT. Further technological improvements are necessary to demonstrate silicon spectrometers with specifications necessary for OCT ($\geq$512 channels, $\leq$0.2 nm resolution). While the first step toward an on-chip SS-OCT is to optimize the passive structures, in the long term, integration with active components will open new application opportunities. Wafer-scale integration of germanium photodetectors on silicon has recently been demonstrated [18]. An interferometer design similar to the one presented in this study can be integrated with such on-chip photodetectors and used for balanced SS-OCT. Integrating the photodetectors will also eliminate the chip-to-fiber losses for the light sent to the photodetectors. Integration of a tunable laser and other active elements (e.g., optical amplifier, modulator) can be pursued by bonding prefabricated components on top of the passive structures or by bonding the active material epitaxial layers on top of the passive waveguides and then processing the active components [6].

Considering state-of-the-art silicon photonic components, including integrated photodetectors, an integrated interferometer for SS-OCT with sensitivity close to fiber interferometers could be realized. The major loss (for light returning from the sample) will be the 3 dB loss at coupler C2, as broadband integrated circulators have not matured yet. Additional 1–2 dB loss at the chip to collimating lens interface and 0.5 dB propagation loss could be present.

In conclusion, we have fabricated and characterized a silicon-based, integrated photonics interferometer for swept-source OCT. We have demonstrated cross-sectional imaging of a layered tissue phantom showing the feasibility and potential of integrated silicon-based OCT systems. Thanks to the small size of the silicon photonic integrated components, silicon photonics can become a platform for highly parallel OCT systems. Monolithic/hybrid integration of active components with passive structures can enable an on-chip OCT system at low cost and small form factor.

This work was supported by Gent University–Methusalem project, “Smart Photonic Chips,” and the IOP Photonics Devices program managed by Agentschap NL. We would like to thank Dr. Dirk J. Faber for helpful discussions.

References

1. D. Huang, E. A. Swanson, C. P. Lin, J. S. Schuman, W. G. Stinson, W. Chang, M. R. Hee, T. Flotte, K. Gregory, C. A. Puliafito, and J. G. Fujimoto, Science **254**, 1178 (1991).
2. B. I. Akca, B. Považay, A. Alex, K. Wörhoff, R. M. de Ridder, W. Drexler, and M. Pollnau, Opt. Express **21**, 16648 (2013).
3. V. Duc Nguyen, N. Weiss, W. Beeker, M. Hoekman, A. Leinse, R. G. Heideman, T. G. van Leeuwen, and J. Kalkman, Opt. Lett. **37**, 4820 (2012).
4. G. Yurtsever, B. Považay, A. Alex, B. Zabihian, W. Drexler, and R. Baets, Biomed. Opt. Express **5**, 1050 (2014).
5. S. K. Selvaraja, P. De Heyn, G. Winroth, P. Ong, G. Lepage, C. Cailler, A. Rigny, K. Bourdelle, W. Bogaerts, D. Van Thourhout, J. Van Campenhout, and P. Absil, in *Optical Fiber Communication Conference*, OSA Technical Digest (online) (Optical Society of America, 2014), paper Th2A.33.
6. H. Park, M. N. Sysak, H. W. Chen, A. W. Fang, D. Liang, L. Liao, B. R. Koch, J. Bovington, Y. Tang, K. Wong, M. Jacob-Mitos, R. Jones, and J. E. Bowers, IEEE J. Sel. Top. Quantum Electron. **17**, 671 (2011).
7. J. S. Orcutt, B. Moss, C. Sun, J. Leu, M. Georgas, J. Shainline, E. Zgraggen, H. Li, J. Sun, M. Weaver, S. Urošević, M. Popović, R. J. Ram, and V. Stojanović, Opt. Express **20**, 12222 (2012).
8. D. Vermeulen, Y. De Koninck, Y. Li, E. Lambert, W. Bogaerts, R. Baets, and G. Roelkens, Opt. Express **20**, 22278 (2012).
9. http://www.epixfab.eu/.
10. H. Yun, W. Shi, Y. Wang, L. Chrostowski, and N. A. F. Jaeger, Proc. SPIE **8915**, 89150V (2013).
11. M. R. Watts, J. Sun, C. DeRose, D. C. Trotter, R. W. Young, and G. N. Nielson, Opt. Lett. **38**, 733 (2013).
12. M. Wojtkowski, V. Srinivasan, T. Ko, J. Fujimoto, A. Kowalczyk, and J. Duker, Opt. Express **12**, 2404 (2004).
13. N. Weiss, T. G. van Leeuwen, and J. Kalkman, Phys. Rev. E **88**, 042312 (2013).
14. T. Bajraszewski, M. Wojtkowski, M. Szkulmowski, A. Szkulmowska, R. Huber, and A. Kowalczyk, Opt. Express **16**, 4163 (2008).
15. D. Vermeulen, S. Selvaraja, P. Verheyen, G. Lepage, W. Bogaerts, P. Absil, D. Van Thourhout, and G. Roelkens, Opt. Express **18**, 18278 (2010).
16. B. Ben Bakir, A. V. de Gyves, R. Orobtchouk, P. Lyan, C. Porzier, A. Roman, and J.-M. Fedeli, IEEE Photon. Technol. Lett. **22**, 739 (2010).
17. K. Shiraishi, H. Yoda, and C. S. Tsai, Opt. Express **20**, 24370 (2012).
18. S. Assefa, F. Xia, W. Green, C. Schow, A. Rylyakov, and Y. Vlasov, IEEE J. Sel. Top. Quantum Electron., **16**, 1376 (2010).